Multicompartment cell-based modeling of confined migration: regulation by cell intrinsic and extrinsic factors

Sandeep Kumar, Alakesh Das, and Shamik Sen*
Department of Biosciences and Bioengineering, IIT Bombay, Mumbai 400 076, India

ABSTRACT Though cell and nuclear deformability are expected to influence efficiency of confined migration, their individual and collective influence on migration efficiency remains incompletely understood. In addition to cell intrinsic properties, the relevance of cell extrinsic factors on confined migration, if any, has not been adequately explored. Here we address these questions using a statistical mechanics-based stochastic modeling approach where cell/nuclear dimensions and their deformability are explicitly taken into consideration. In addition to demonstrating the importance of cell softness in sustaining confined migration, our results suggest that dynamic tuning of cell and nuclear properties at different stages of migration is essential for maximizing migration efficiency. Our simulations also implicate confinement shape and confinement history as two important cell extrinsic regulators of cell invasiveness. Together, our findings illustrate the strength of a multicompartment model in dissecting the contributions of multiple factors that collectively influence confined cell migration.

INTRODUCTION

Cell migration is a fundamental process pivotal to physiological as well as pathological conditions. Dysregulation of cell migration can lead to developmental defects and diseased conditions including cancer (Franz *et al.*, 2002). During three-dimensional cell migration, that is, migration through interstitial matrices, cells must overcome the steric hindrance provided by the matrix. To circumvent this steric hindrance, cells secrete proteases that degrade the matrix, thereby enlarging pores and enabling cell migration (Wolf *et al.*, 2007; Friedl and Wolf, 2009). Alternatively, in cells that are incapable of degrading the extracellular matrix (ECM), cells must squeeze through preexisting pores in the matrix (Wolf *et al.*, 2003;

Lammermann and Sixt, 2009; Friedl and Wolf, 2010). For these cases, successful migration presumably requires both the cell and the nucleus to be soft to enable rapid changes in cell/nuclear shape (Wolf *et al.*, 2013; Krause and Wolf, 2015).

Given the necessity of increased cell/nuclear deformability for migration through matrices, it is perhaps not surprising that highly invasive cancer cells that metastasize to distant organs are often softer than their nontransformed counterparts. Indeed, cell softening has been linked with higher cancer invasiveness and higher metastasis efficiency (Swaminathan *et al.*, 2011; Plodinec *et al.*, 2012; Xu *et al.*, 2012). However, cell softening may not be sufficient in sustaining invasion through dense interstitial matrices, where nuclear squeezing represents the rate-limiting factor as the nucleus cannot be deformed below 10% of its uncompressed size (Wolf *et al.*, 2013; Krause *et al.*, 2013; McGregor *et al.*, 2016). Loss of lamin A/C, the major nuclear envelope protein dictating physical properties of the nucleus (Dahl *et al.*, 2008), has been shown to promote cell migration under confinement through increased nuclear deformability (Davidson *et al.*, 2014, 2015; Harada *et al.*, 2014).

While the above studies illustrate the individual importance of cell and nuclear deformability in dictating migration through confined environments, their relative importance remains unclear. Further, it is likely that the extent of confinement determines the individual influence of these parameters on cell invasiveness. In addition,

the geometry of confinement may also provide additional cues that enhance or inhibit cancer invasiveness. Experimentally probing the contributions of these individual components on cell invasion remains a challenge due to the large parameter space. Additionally, given the physical coupling between the cell and its nucleus, independent modulation of either cell stiffness or nuclear stiffness is experimentally challenging, thereby making it difficult to discern their individual importance during invasion. In such cases, computational modeling approaches where properties of the cell and the nucleus can be accounted for and independently tuned represent a useful alternative to augment experimental studies. Of the multiple mathematical formalisms, Monte Carlo simulation-based cellular Potts modeling (CPM) approach is particularly well suited to study deformable entities and has been used to study many important phenomena including collective cell migration (Kabla, 2012; Vedula et al., 2012; Doxzen et al., 2013), angiogenesis (Bauer et al., 2009), tumor growth (Sottoriva et al., 2011), cell spreading/patterning (Kafer et al., 2007; Szabo and Merks, 2013; Boghaert et al., 2014; Albert and Schwarz, 2016), and cancer invasion (Szabo et al., 2012; Kumar et al., 2016).

In this article, we have used multicompartment CPM to develop a computational model of confined cell migration that accounts for cell/nuclear dimensions and their stiffness. By simulating migration of a multicompartment cell through channels of different sizes, we show that cell softening is critical for sustaining migration in confined environments, with additional nuclear softening required when migrating through subnuclear sized channels. Interestingly, our results suggest that the requirements of cell/nuclear stiffness during cell entry into channel and transit through the channel are distinct. Our findings also implicate confinement shape and confinement geometry as two important cell extrinsic factors that influence invasion efficiency, with gradual increase in extent of confinement fostering migration and sharp increase in confinement inhibiting migration. This study also demonstrates that confinement history, that is, the extent of confinement witnessed by a cell in recent past, also influences the efficiency of cell invasion. Taken together, our results suggest that cell/nuclear deformability, confinement architecture, and confinement history collectively regulate invasion efficiency.

RESULTS
Multicompartment model of cell migration under confinement
For probing the relative importance of cell and nuclear softening on protease-independent migration through confined environments, we developed a Monte Carlo simulation-based CPM (Swat et al., 2012), which allows independent control of cell and nuclear deformability. While several computational models have been developed for exploring confined cell migration, most of these models do not account for the properties of the nucleus, which being the stiffest and the largest organelle inside the cell, is expected to majorly influence migration efficiency (Wolf et al., 2013; Krause and Wolf, 2015; Davidson et al., 2015; Lautscham et al., 2015; McGregor et al., 2016). In this work, using a multicompartment modeling approach, we have developed a computational framework that provides independent control of cytoplasmic and nuclear deformability thereby facilitating exploration of nuclear dynamics during confined migration. In our model, cell was modeled as a nine-compartment entity with the center compartment representing the nucleus and the remaining eight compartments representing the cytoplasm (Figure 1A). Each compartment area was estimated to be 25 μm^2 based on experimentally determined average

spread area of MDA-MB-231 cells (Supplemental Figure S1, A and B; see *Materials and Methods* for details). To model cytoplasmic and nuclear deformability, all the compartments were allowed to change their position and shape over time, retaining the connectivity between the individual components. To control the extent of deformability, all compartments were subjected to area and perimeter constraints, with area constraint modeling the effect of bulk stiffness and perimeter constraint modeling line tension (Fletcher et al., 2013). While the area constraint prevents a compartment from becoming too large or too small, the perimeter constraint of a compartment ensures that the compartment does not undergo excessive deformations (Swat et al., 2012; Kumar et al., 2016).

To independently control cell and nuclear deformability, we selectively varied the area/perimeter constraints of the cytoplasmic compartments ($\lambda_{a,C}$ or $\lambda_{p,C}$) and the nucleus compartment ($\lambda_{a,N}$ or $\lambda_{p,N}$), with these parameters influencing cell/nuclear stiffness. Since experimentally measured estimates of nuclear stiffness (2–6 kPa) were higher than that of cell stiffness (0.5–2.5 kPa) (Supplemental Figure S1, C–E), we assumed $\lambda_{a,C} \leq \lambda_{a,N}$ and $\lambda_{p,C} \leq \lambda_{p,N}$ in our simulations with max($\lambda_{a,C}$) = 0.5 × max ($\lambda_{a,N}$) and max($\lambda_{p,C}$) = 0.5 × max ($\lambda_{a,N}$). The different combinations of ($\lambda_{a,C}$, $\lambda_{a,N}$) and ($\lambda_{p,C}$, $\lambda_{p,N}$) allowed us to generate different cell/nuclear phenotypes (Figure 1B; Supplemental Videos V1–V3). To assess the sensitivity of cell and nuclear deformability to cell/nuclear constraints, we quantified the extent of variation (i.e., SD) in cell volume and nuclear volume for different combinations of area constraints, that is, ($\lambda_{p,C}$, $\lambda_{p,N}$) and perimeter constraints, that is, ($\lambda_{p,C}$, $\lambda_{p,N}$). As expected, increase in perimeter and area constraints led to decrease in fluctuations of cell/nuclear volume with ≈20% drop in cell volume fluctuation and a 28% drop in nuclear volume fluctuation observed on increasing ($\lambda_{p,C}$, $\lambda_{p,N}$) from its lowest considered value (i.e., (2,2) E/L^2) to its highest considered values (i.e., (10,20) E/L^2) (Figure 1C). Comparatively, a stronger influence of cell/nuclear area constraint was observed on cell/nuclear volume fluctuations (Figure 1D).

To model cell migration under confinement, a two-dimensional computational model was developed wherein a multicompartment cell (as described above) was allowed to transit through a 300-μm-long channel of defined width (ϕ = 3, 5, 7, and 17 μm) (Figure 1E). Our computational model closely resembles microfluidic channels used for studying confined cell migration and for visualizing nuclear deformations during migration through confined environments (Davidson et al., 2014, 2015). In vivo, such situations can arise during cell migration at tissues interfaces (Weigelin et al., 2012; Alexander et al., 2013). Because chemotaxis represents one of the major directional forces that facilitates such motion (Roussos et al., 2011), in this work, constant gradient-directed cell migration was simulated. Spatiotemporal evolution of the simulation lattice was governed by random movement of individual pixels subjected to transition probabilities based on the Monte Carlo method (Swat et al., 2012; Kumar et al., 2016). In brief, two neighbor pixels are selected randomly and one of the pixel is moved to other one (called copy-index event; refer to *Materials and Methods*) (Supplemental Figure S2A). The change in energy ΔE caused by this random move is calculated and the move is accepted if ΔE ≤ 0. Otherwise, the proposed move is accepted with probability p given by

$\exp\left(-\dfrac{\Delta E}{k_B T}\right)$ (Supplemental Figure S2B). The developed model was implemented using the freely available open-source software package CompuCell3D (CC3D) (Swat et al., 2012) and custom-written Python scripts. Refer to *Materials and Methods* and the Supplemental Material for further details.
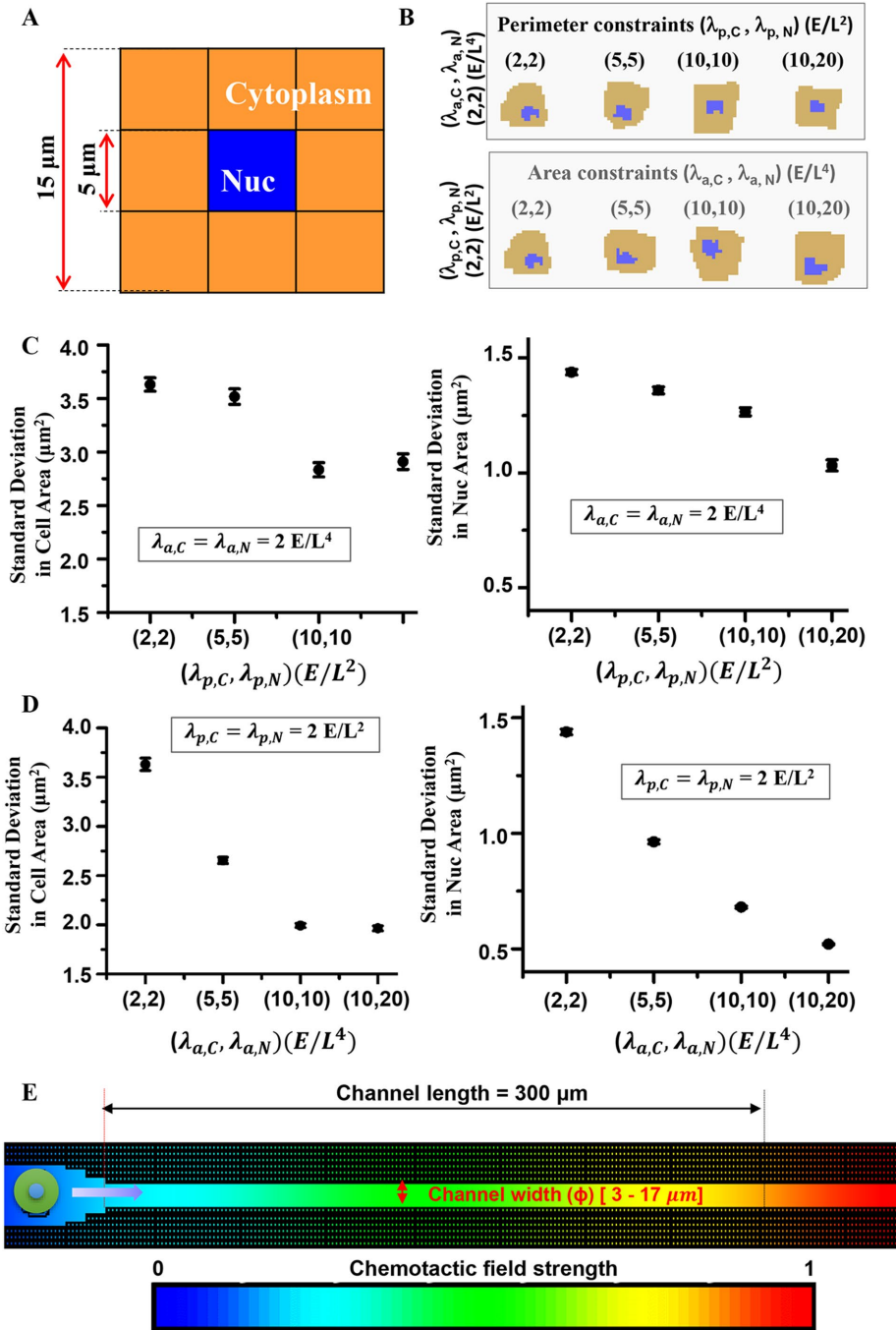
FIGURE 1: Multicompartment model of a single cell taking size, shape, and stiffness of the cell and nucleus into consideration. (A) Cell was modeled as a nine-compartment entity with the central compartment representing the nucleus (blue) and the other eight compartments representing the cytoplasm (orange). (B, top panel) Representative cell/nuclear phenotypes for various combinations of cell perimeter constraint ($\lambda_{p,C}$) and nuclear perimeter constraint ($\lambda_{p,N}$). (B, bottom panel) Representative cell/nuclear phenotypes for various combinations of cell area constraint ($\lambda_{a,C}$) and nuclear area constraint ($\lambda_{p,N}$). On the basis of our experimental data, we assumed that $\lambda_{p,N} \geq \lambda_{p,C}$ and $\lambda_{p,N} \geq \lambda_{p,C}$. (C, left) Standard deviation in cell area for four different combinations of $\lambda_{p,C}$ and $\lambda_{p,N}$. (C, right) Standard deviation in nuclear area for four different combinations of $\lambda_{p,C}$ and $\lambda_{p,N}$. (D, left) Standard deviation in cell area for four different combinations of $\lambda_{p,C}$ and $\lambda_{p,N}$. (D, right) Standard deviation in nuclear area for four different combinations of $\lambda_{p,C}$ and $\lambda_{p,N}$. (E) Chemotaxis-mediated cell migration through varying extents of confinement was simulated by allowing a cell to migrate though a 300-μm-long channel of various widths (ϕ).

Computational simulations predict differential sensitivity of entry efficiency to cell and nuclear deformability

Previous studies have demonstrated that cell and nuclear deformability play important roles in sustaining migration through dense interstitial matrices (Rowat *et al.*, 2013; Wolf *et al.*, 2013; Lautscham *et al.*, 2015). However, it is experimentally challenging to dissect the individual and collective contributions of cell and nuclear deformability in influencing cell invasiveness. To address this, simulations were performed for four different values of channel sizes, that is, $\phi = (3, 5, 7, 17)$ μm, and nine different combinations of cell/nuclear perimeter constraints, that is, ($\lambda_{p,C}, \lambda_{p,N}$) = (2,2), (2,5), (2,10), (2,20), (5,5), (5,10), (5,20), (10,10), (10,20) E/L^2. In these simulations, cell/nuclear area constraints were kept constants at ($\lambda_{a,C}, \lambda_{a,N}$) = (2,2) E/L^4. At least 100–200 simulations for each of the 36 scenarios (=4 values of ϕ * 9 combinations of cell/nuclear stiffness) were performed where cell migration through the confined channel was simulated for 40 h and position of the cell at the end of the simulation was extracted to quantify the extent of invasiveness of the cell.

At the end of the simulations, a cell can 1) be at the start of the channel, signifying that it could not enter the channel (Supplemental Video V4); 2) be inside the channel, signifying that cell entered the channel but could not pass through the channel (i.e., got trapped inside the channel) (Supplemental Video V5); or 3) have reached the channel end-point, signifying that cell entered the channel and transited through the channel successfully (Supplemental Video V6) (Figure 2A). From the end position of the cells, we quantified *entry efficiency* defined as the percentage of cases the cell successfully entered the channel. For the cases where the cell entered the channel, in a proportion of cases, the cell got trapped inside the channel (Figure 2B, red), while for the remaining cases, the cell successfully transited the channel (Figure 2B, green). Near complete trapping inside the channel for $\lambda_{p,C} = 10 \frac{E}{L^2}$ demonstrates the role of cell deformability in modulating invasion efficiency (Figure 2B). In channels of widths less than nuclear dimensions (i.e., $\phi = 3$ μm), in ≥50% of the cases, the cell was unable to enter the channel. This observation is in agreement with an experimental study wherein ~50% drop in invasion
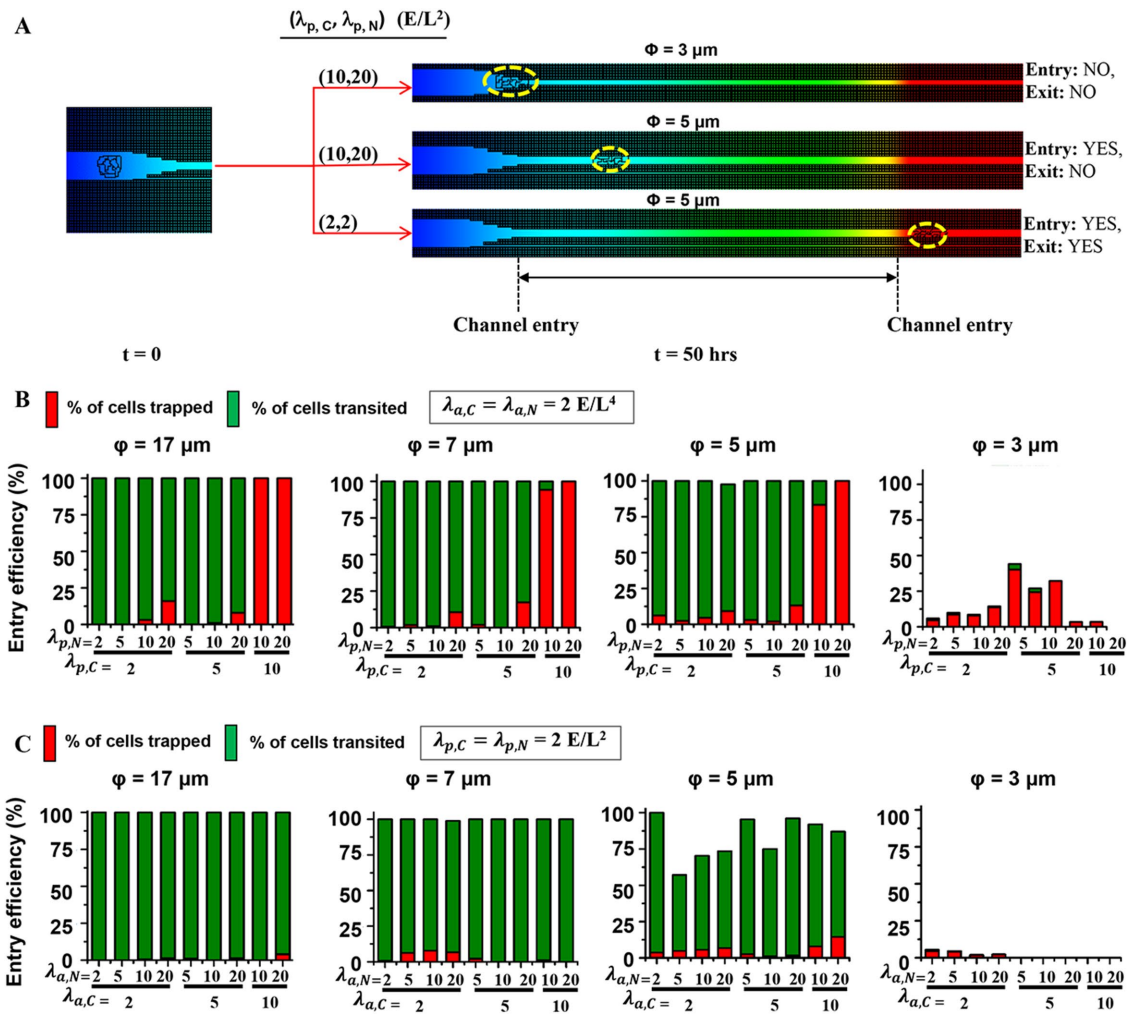
FIGURE 2: Cell entry efficiency for different values of cell and nuclear deformability. (A) Schematic showing the initial position and final position(s) of a cell migrating through a confined channel for three different combinations of perimeter constraints $(\lambda_{p,C}, \lambda_{p,N})$: 1) cell failed to enter the channel for $(\lambda_{p,C}, \lambda_{p,N}) = (10,20)\, E/L^2$ and $\phi = 3\,\mu m$, 2) cell entered the channel but got stuck inside the channel for $(\lambda_{p,C}, \lambda_{p,N}) = (10,20)\, E/L^2$ and $\phi = 5\,\mu m$, and 3) cell successfully exited the channel for $(\lambda_{p,C}, \lambda_{p,N}) = (2,2)\, E/L^2$ and $\phi = 5\,\mu m$. (B) Statistics of entry efficiency into channels of various widths for different combinations of $(\lambda_{p,C}, \lambda_{p,N})$. Data were collected from 100 to 200 simulations per condition. Red denotes the percentage of cases where the cell entered the channel but got stuck inside. Green denotes the percentage of cases where the cell successfully exited the channel. (C) Statistics of entry efficiency into channels of various widths for different combinations of cell/nuclear area constraints $(\lambda_{p,C}, \lambda_{p,N})$.

efficiency was observed when pore size was decreased from 8 to 3 μm (Rowat *et al.*, 2013). Intriguingly, highest cell entry was observed at moderate cell/nuclear perimeter constraints, suggesting that too-soft or too-stiff cells are unfit to invade through confinement smaller than nuclear size. While this may be attributed to loss of directionality for the case of very soft cells, for the case of very stiff cells it may be due to their inability to deform (Figure 1B). Additionally, in line with experimental findings (Balzer *et al.*, 2012), cell length was found to increase with increasing extent of confinement (Supplemental Figure S3). Such stretching of the cell under confinement is a consequence of cell area/perimeter constraints used in our formalism that ensure an approximately fixed cell size. When migrating through channels wider than cell dimensions, the cell was observed to preferably migrate along one wall (Supplemental Video V7), which has also been observed experimentally (Paul *et al.*, 2016).

While the above results provide insights on the influence of cell/nuclear perimeter constraints (i.e., $\lambda_{p,C}$ and $\lambda_{p,N}$) on cell entry efficiency, cell/nuclear area constraints were kept constants in these simulations. While both area and perimeter constraints are expected to influence cell deformability (Swat *et al.*, 2012), no systematic study has been performed to assess the relative importance of these two constraints. To probe if cell/nuclear area constraints influence entry efficiency similar to that of cell/nuclear perimeter constraints, simulations were performed for nine combinations of cell/nuclear area constraints, that is, $(\lambda_{a,C}, \lambda_{a,N}) = (2,2), (2,5), (2,10), (2,20), (5,5),$ $(5,10), (5,20), (10,10), (10,20)\, E/L^4$. Cell/nuclear perimeter constraints were kept constant at the lowest values, that is, $(\lambda_{p,C}, \lambda_{p,N}) = (2,2)\, E/L^2$. Quantification of migration trajectories revealed that, in contrast to above simulations with various perimeter constraints, increase in area constraints did not appreciably alter entry efficiency, except in channels smaller than nuclear dimensions where entry
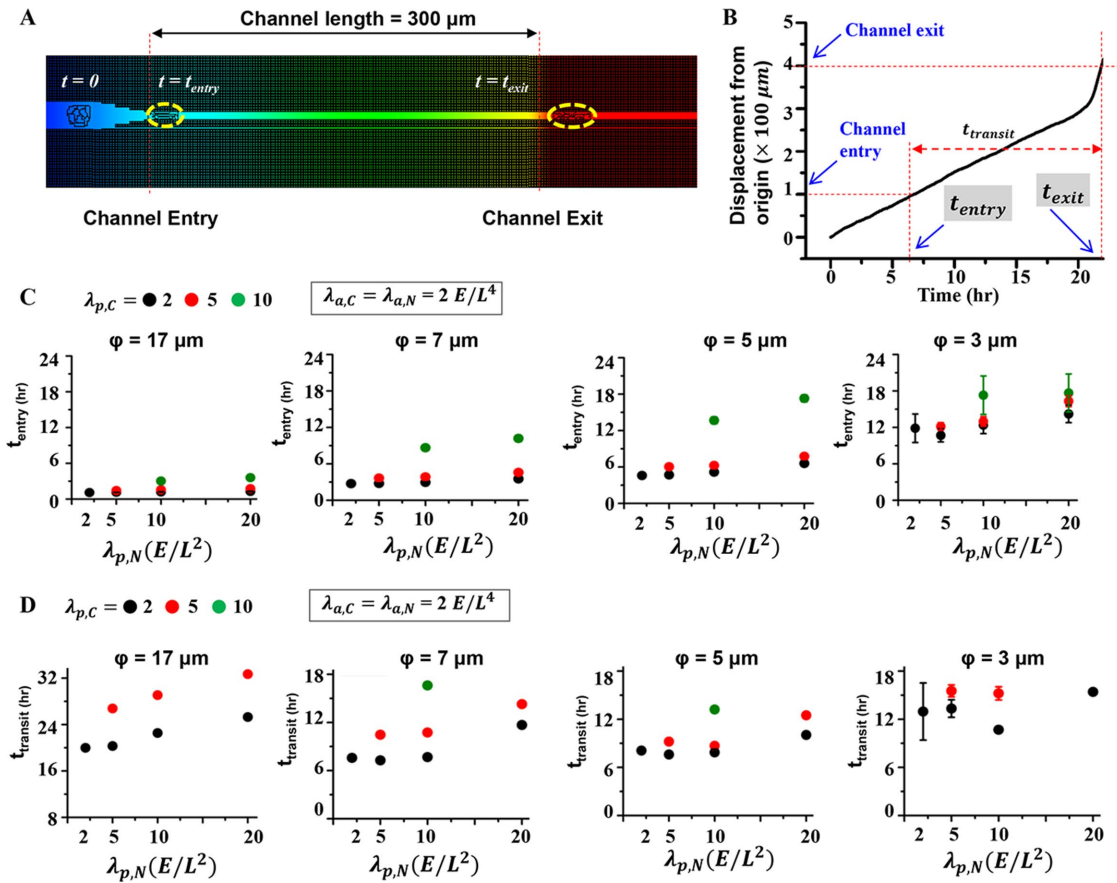
FIGURE 3: Influence of cell and nuclear deformability on invasion efficiency. (A) Schematic showing position of the cell at the start of the simulations, at the point of channel entry, and at the point of channel exit. (B) A representative trajectory of the cell showing the distance traveled by the cell centroid from its original position as a function of time. t_{entry} represents the time at which the cell centroid crosses the channel entry point. t_{exit} represents the time at which the cell exits the 300-μm-long channel. $t_{transit}$ represents the total time taken by the cell to reach from entry point to exit point. (C) Statistics of t_{entry} for various combinations of perimeter constraints ($\lambda_{p,C}$, $\lambda_{p,N}$) and different channel widths. Area constraints were kept fixed at ($\lambda_{a,C}$, $\lambda_{a,N}$) = (2, 2) E / L^4. (D) Statistics of $t_{transit}$ for various combinations of perimeter constraints ($\lambda_{p,C}$, $\lambda_{p,N}$) and different channel widths. Area constraints were kept fixed at ($\lambda_{a,C}$, $\lambda_{a,N}$) = (2, 2) E / L^4. Error bars: ± SEM.

efficiency was nearly zero for all values of area constraints (Figure 2C). In addition to revealing the expected dependence of entry efficiency on the extent of confinement, these results are indicative of a greater sensitivity of entry efficiency to cell deformability, with a stronger dependence on perimeter constraint compared with area constraint.

Influence of cell/nuclear deformability on invasion efficiency
To further probe the dependency of invasion efficiency on cell and nuclear deformability, for the cases when the cell successfully entered the channel, migration trajectories of the cell were analyzed to determine *entry time* (t_{entry}), that is, the time required to enter the channel from the start of the simulations (Figure 3A). To calculate t_{entry}, we tracked the displacement of the cell centroid from its initial position to the time when it crosses the channel entry (Figure 3B). In simulations performed with constant area constraints and various perimeter constraints, for channels comparable or larger than the nucleus ($\phi \leq 5$ μm), entry time was insensitive to nuclear stiffness and dictated solely by celvl stiffness (Figure 3C). This effect of cell stiffness was even more pronounced with increase in the extent of confinement (i.e., lower values of ϕ). In channels of sizes smaller than

nuclear size ($\phi = 3$ μm), entry time increased only when nuclear stiffness was increased to its maximum value, that is, $\lambda_{p,N} = 20\frac{E}{L^2}$.

Next, to determine the influence of cell and nuclear deformability on overall invasion efficiency, statistics of *transit time* ($t_{transit}$), that is, time spent between entry point and exit point (Figure 3, A and B), was obtained from the cases where the cell successfully transited the channel (Figure 2A, right bottom). While $t_{transit}$ increased with increase in cell stiffness (Figure 3D), the strength of this dependence was set by the extent of confinement, with maximum sensitivity to cell stiffness observed for the widest channel ($\phi = 17$ μm). Transit time also exhibited a dependence on nuclear stiffness, with highest transit time observed for cells with stiffest nucleus (i.e., $\lambda_{p,N} = 20\frac{E}{L^2}$). This is consistent with experimental findings where 20- to 30-fold increase in expression levels of the nuclear membrane protein lamin A that dictates stiffness of the nuclear membrane (Lammerding *et al.*, 2004; Lammerding *et al.*, 2006; Pajerowski *et al.*, 2007) has been shown to cause a threefold increase in passage time of modified HL-60 lukemia cells when migrating through 5-μm constrictions (Rowat *et al.*, 2013). For the same combinations of cell and nuclear stiffness, for majority of the

cases, higher transit time was observed with decrease in channel size.

Since cell/nuclear area constraints were kept constant in the above simulations, we next performed simulations for various area constraints but constant perimeter constraints (($\lambda_{p,C}$, $\lambda_{p,N}$) = (2,2) E/L^2) (Supplemental Figure S4). Both entry time and transit time were nearly insensitive to nuclear area constraint and only mildly sensitive to cell area constraint (Supplemental Figure S4). Together, these results suggest that compared with nuclear deformability, cell deformability exhibits a much stronger influence on invasion efficiency.

Given the reduction in invasion efficiency with increase in the extent of confinement (i.e., increase in transit time with reduction in channel width), we next asked if confinement-dependent dynamic tuning of cell/nuclear deformability might be a strategy utilized by cells during migration through tight spaces. Elevated levels of actomyosin contractility—which mediates nuclear translocation through tight spaces (Wolf *et al.*, 2013)—can cause buckling and subsequent fragmentation of actin filaments, thereby leading to cell softening (Murrell and Gardel, 2012; Vogel *et al.*, 2013). Given the viscoelastic nature of the nucleus (Pajerowski *et al.*, 2007), migration through confined spaces is also expected to reduce the effective nuclear stiffness over time. Nuclear rupture events observed during migration through highly confined regions (Denais *et al.*, 2016; Raab *et al.*, 2016) may represent another prospective mechanism of confined migration by transient softening of the nucleus. To test if confinement-dependent tuning of cell/nuclear stiffness can indeed increase cell invasiveness, simulations were performed wherein a cell migrated through a long stepped channel comprising four regions each 70 μm in length. The channel widths of the four regions were ϕ = 17, 11, 7, and 5 μm, respectively (Supplemental Figure S5A). For simulating dynamic tuning of cell/nuclear properties, the area constraints were assumed to decrease from $\lambda_{a,C} = \lambda_{a,N} = 10 \frac{E}{L^4}$ in the first segment of the channel (i.e., ϕ = 17 μm) to $\lambda_{a,C} = \lambda_{a,N} = 2 \frac{E}{L^4}$ in the last segment of the channel (i.e., ϕ = 5 μm). For these simulations, the perimeter constraints were kept constant. Transit times were then computed for the middle 50-μm segment in each of the four regions. Compared to the case of constant area constraints ($\lambda_{a,C} = \lambda_{a,N} = 10 \frac{E}{L^4}$), confinement-dependent dynamic tuning of cell/nuclear properties led to increased invasiveness with ≈40% lower transit time observed in the narrowest 5-μm region (Supplemental Figure S5B).

Influence of confinement geometry on invasion efficiency

To enter into highly confined channels, cells must continuously change their shape. While cell deformability is essential, confinement geometry itself may also play an important role in enabling shape changes, thereby influencing entry efficiency. To probe the effect of confinement shape on entry efficiency, we compared efficiency of cell entry into a channel of size ϕ = 5 μm for two different confinement geometries. Of these, the tapered geometry as used before is expected to serve as a guidance cue thereby enabling cells to enter the channels (Figure 4A). Such a guidance cue is absent for the case of the channel with flat entry (Figure 4B). Consistent with our reasoning, in contrast to the tapered channel where entry efficiency was ~100% (Figure 2B), <75% of cells were able to enter the channel with flat geometry (Figure 4C). Also, cells took significantly more time to enter into flat channels compared with tapered channels for all four combinations of cell and nuclear perimeter constraints (Figure 4D). While entry times were comparable for both the geometries for stiff cell/nucleus (i.e., ($\lambda_{p,C}$, $\lambda_{p,N}$) ≥ (10,10) E/L^2), entry

into tapered channels is significantly faster compared with flat channels when cell/nucleus were soft (i.e., ($\lambda_{p,C}$, $\lambda_{p,N}$) ≤ (5,5) E/L^2) (Figure 4D). Faster entry in tapered channels at lower perimeter constraints can be attributed to the fact that deformable cells (i.e., cells with lower perimeter constraints) can more effectively change their shape under confinement. As intuitively expected, no difference in transit time was observed for the two different channel shapes (Supplemental Figure S6).

Since our previous results revealed that area constraints influence entry efficiency in a way different than perimeter constraints (Figure 2, B and C), simulations were performed where area constraints were varied and perimeter constraints were kept constant. Entry efficiency into flat channels dropped significantly with increase in area constraint (Figure 4E). Additionally, in contrast to the nonlinear dependence of entry time on perimeter constraint observed in the case of tapered channels, entry time exhibited a gradual increase with increasing area constraint (Figure 4F). Collectively, these results suggest that when cells are compliant, appropriate confinement geometry can enhance cell invasiveness by providing suitable guidance cues.

Influence of confinement history on entry efficiency

In the above simulations, faster entry into tapered channels illustrates the importance of guidance cues in influencing invasion efficiency by effecting gradual changes in cell/nuclear shape leading to the final squeezed state. However, the extent to which this squeezing influences cell invasiveness at later time points remains unclear. We hypothesize that cell invasiveness of a squeezed cell at later time points is dictated by the timescale of its relaxation. To test this, simulations were performed wherein cell migration through a channel with a confined region was followed by an unconfined region, that is, region with width larger than the cell diameter (Figure 5A). Relaxation of the cell was tracked by quantifying the total cell area as a function of time. Simulations were performed for four different combinations of cell/nuclear area constraints, that is, ($\lambda_{a,C}$, $\lambda_{a,N}$) = (2,2), (5,5), (10,10), (10, 20) E/L^4, with cell/nuclear perimeter constraints kept constant at ($\lambda_{p,C}$, $\lambda_{p,N}$) = (2,2) E/L^2. Temporal dynamics of cell area revealed the existence of a characteristic timescale of relaxation (t_{relax}) and a characteristic length scale of relaxation (d_{relax}) (Figure 5A, bottom panel). While t_{relax} corresponds to the time taken by the cell to regain its unconfined area after exiting the confined region, d_{relax} corresponds to the distance travelled by the cell during this time. Somewhat surprisingly, both t_{relax} and d_{relax} were mildly sensitive to cell/nuclear deformability (Figure 5, B and C), with t_{relax} ~ 205 h and d_{relax} ~ 35 μm.

To next probe the extent to which partial squeezing of the cell impacts its invasiveness at later times, simulations were performed where a cell migrated through a channel having two confined regions (ϕ = 5 μm) separated by an unconfined region of width ϕ = 17 μm and length d_{GAP} (Figure 5D, Supplemental Videos V8 and V9). d_{GAP} was varied in these simulations to determine if entry efficiency is higher when $d_{GAP} \leq d_{relax}$. For these simulations, moderate values of area constraints (i.e., ($\lambda_{a,c}$, $\lambda_{a,N}$) = (5,5) E/L^4) and the lowest values of perimeter constraints (i.e., ($\lambda_{p,C}$, $\lambda_{p,N}$) = (10,10) E/L^2) were used. Consistent with our line of reasoning, entry efficiency was >75% as long as the separation between two confined regions was smaller than d_{relax} (Figure 5E). Beyond this length scale, entry efficiency dropped with further increase in d_{GAP} with ≈50% efficiency for d_{GAP} = 75 μm. Together, these results suggest that in addition to current state of confinement, the extent of confinement experienced by invading cells in recent past also influences cell invasiveness.
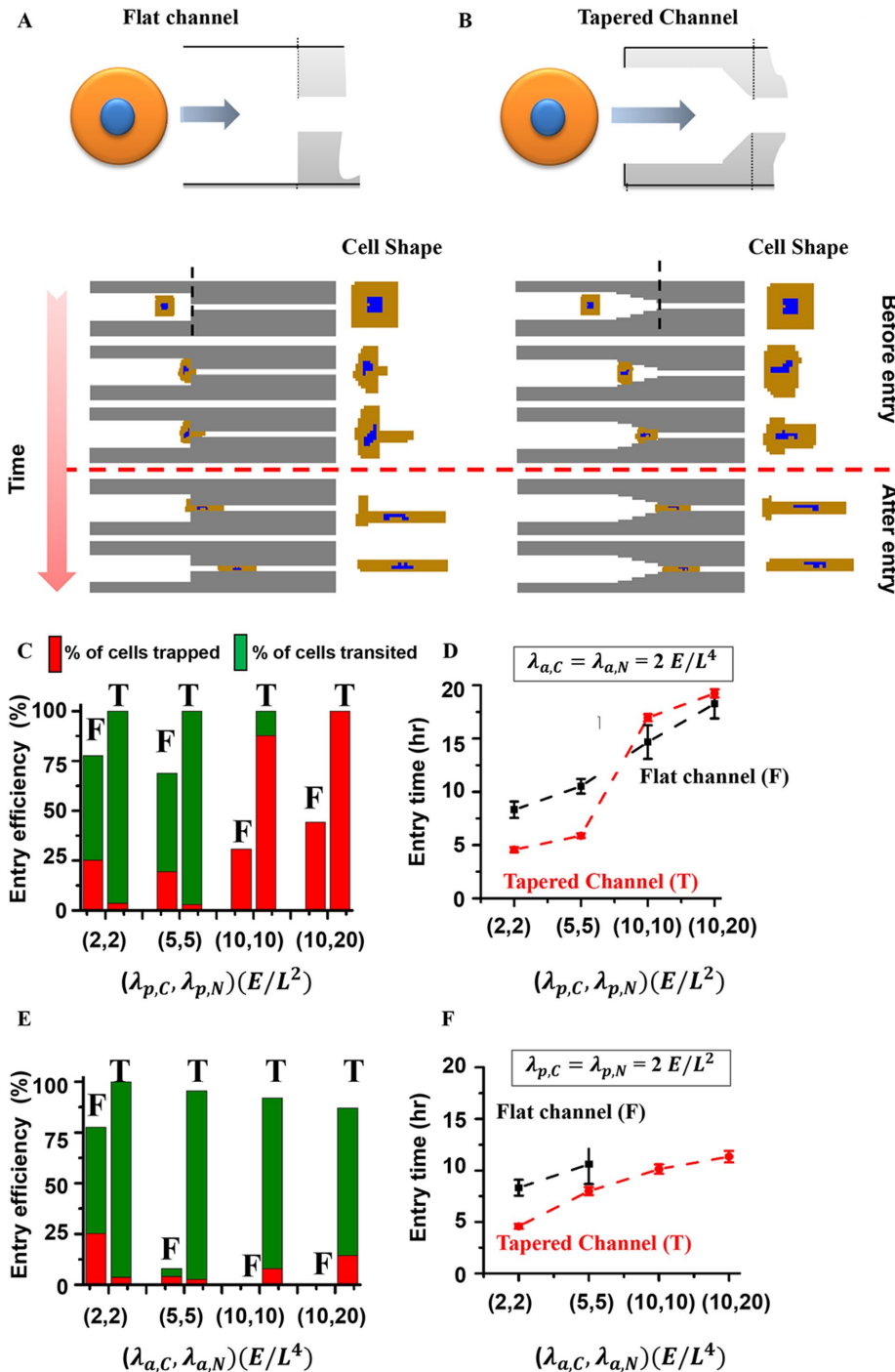
FIGURE 4: Cell entry into channels of different shape. (A, top) Channel with tapered shape at entry. (A, bottom) Time evolution of cell shape during migration through a 5-µm channel with tapered geometry at entry point. (B, top) Channel with flat shape at entry. (B, bottom) Time evolution of cell shape during migration through a 5-µm channel with flat geometry at entry point. (C) Entry efficiency into tapered and flat channels for four different combinations of cell and nuclear perimeter constraints ($\lambda_{p,C}$, $\lambda_{p,N}$). Red indicates the percentage of cases where the cell got trapped at entry. Green indicates the percentage of cases where the cell successfully transited the channel. (D) Entry times for tapered and flat channels for four different combinations of cell and nuclear perimeter constraints ($\lambda_{p,C}$, $\lambda_{p,N}$). Error bars: ± SEM. (E) Entry efficiency into tapered and flat channels for four combinations of cell and nuclear area constraints ($\lambda_{p,C}$, $\lambda_{p,N}$). Red indicates the percentage of cases where the cell got trapped at entry. Green indicates the percentage of cases where the cell successfully transited the channel. (F) Entry times for tapered and flat channels for four different combinations of cell and nuclear area constraints ($\lambda_{p,C}$, $\lambda_{p,N}$). Error bars: ± SEM.

DISCUSSION

The importance of cell and nuclear deformability on cancer invasiveness is well appreciated. However, their relative importance in dictating invasiveness depending on the extent of confinement has not been fully probed. Here we address this important question computationally using a multicompartment model of a cell that takes into account both cell and nuclear dimensions as well as their deformability. Thus, this model can also be utilized for probing biophysics of diseases such as Hutchinson-Gilford progeria syndrome where physical properties of nucleus are perturbed (Goldman *et al.*, 2004; Verstraeten *et al.*, 2008). While the strength of this approach lies in the ability to independently tune cell/nuclear properties (which is experimentally not possible), as well as extending our model to three dimensions, many other biological aspects (e.g., calcium signalling [Hung *et al.*, 2016]) have not been taken into consideration to keep the model simple. To avoid explosion of parameter space and for keeping our model tractable, we have not incorporated cytoskeletal dynamics (Cano *et al.*, 1991; Pankov *et al.*, 2005; Muller *et al.*, 2016) or accounted for cellular organelles such as Golgi (Nemere *et al.*, 1985; Pouthas *et al.*, 2008; Miller *et al.*, 2009), mitochondria (Desai *et al.*, 2013), and centrosome (Yvon *et al.*, 2002; Luxton and Gundersen, 2011), which have all been reported to influence migration efficiency.

Studies by several research groups have demonstrated that cells can migrate directionally even in the absence of chemokines by alternate mechanisms such as confinement-induced polarization (Balzer *et al.*, 2012; Le Berre *et al.*, 2013; Caballero *et al.*, 2015; Paul *et al.*, 2016), development of polarization due to in-flow of water at the cell front and out-flow of water at the cell rear (Stroka *et al.*, 2014), and cortex-destablization induced fast migration (Irimia and Toner, 2009). However, even in the absence of chemokines, cells can create chemotactic gradients through nonuniform chemokine uptake (Scherber *et al.*, 2012). The current version of the model is not suitable for studying cell migration in the absence of chemokine gradients or with such de novo generated directional cues. Incorporating these aspects in our model represent future directions for extending this work.

Cell invasiveness in three-dimensional environments is dictated by a combination of cell/nuclear size, cell adhesivity, cell contractility, and cell/nuclear stiffness, with cells suitably combining one or more of these
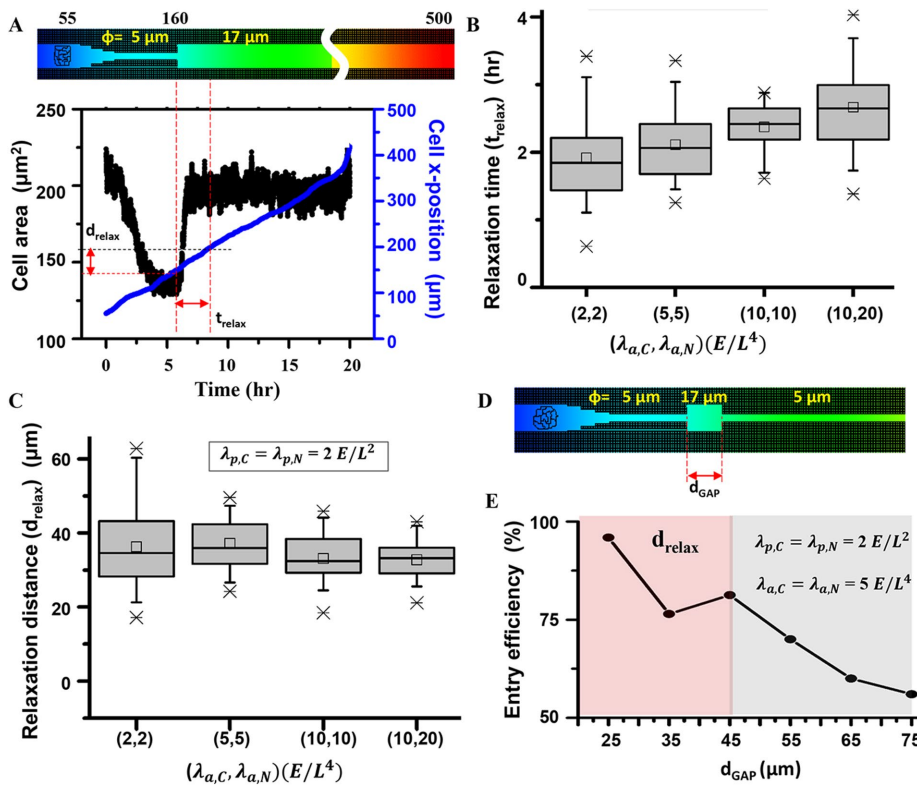
FIGURE 5: Cell migration through confinement of different geometry. (A, top) Cell migration through a channel comprising a confined region ($\phi = 5\ \mu m$) followed by an unconfined region ($\phi = 17\ \mu m$). Bottom, representative trajectory of the cell showing the cell position and cell area as a function of time for $(\lambda_{p,C}, \lambda_{p,N}) = (2,2)\ E/L^2$ and $(\lambda_{p,C}, \lambda_{p,N}) = (2,2)\ E/L^4$. As the cell exits the confined region, it regains its original volume. The relaxation time (t_{relax}) is defined as the time required by the cell to regain its original volume after exiting the confined region. Relaxation distance (d_{relax}) is defined as the distance moved by the cell during t_{relax}. (B, C) t_{relax} and d_{relax} for four different combinations of area constraints ($\lambda_{a,C}, \lambda_{a,N}$). The perimeter constraints were kept fixed at ($\lambda_{p,C}, \lambda_{p,N}$) = (2,2) E/L^2. (D) Cell migration through a channel comprising two confined regions ($\phi = 5\ \mu m$) separated by an unconfined region ($\phi = 17\ \mu m$) of length d_{GAP} (varied in the simulations). (E) Entry efficiency for six different values of d_{GAP} for ($\lambda_{p,C}, \lambda_{p,N}$) = (2,2) E/L^2 and ($\lambda_{p,C}, \lambda_{p,N}$) = (5,5) E/L^4.

ping between area/perimeter constraints with experimentally measured stiffness values is not straightforward, increase in area/perimeter constraints should lead to reduction in invasiveness. For example, higher nuclear perimeter constraints can be correlated with higher expression of the nuclear membrane protein Lamin A/C, making the nucleus less deformable and the cell less invasive, as has been observed experimentally (Rowat et al., 2013).

Tracking temporal dynamics of cell transit through channels allowed us to identify the major bottlenecks that impede cell motility at different stages of confined migration. Requirement of distinct mechanical properties of cell/nucleus at different stages of migration necessitates dynamic tuning of cell and nuclear properties during invasion. Thus, while increased softening has been associated with increased invasiveness (Swaminathan et al., 2011; Plodinec et al., 2012; Xu et al., 2012; Wolf et al., 2013; Krause and Wolf, 2015), our results suggest that some stages of invasion may require moderate cell/nuclear stiffness. Strain stiffening and viscoelastic stress relaxation observed in other biopolymer networks may represent some of the mechanisms by which dynamic alterations in cell and nuclear properties are enabled (Pajerowski et al., 2007; Licup et al., 2015). Though our simulation results demonstrate the utility of confinement-dependent cell/nuclear softening during migration through confined geometries, the existence of such confinement-dependent dynamic phenotypic alterations and identification of underlying mechanisms remains to be established experimentally.

Differences in the metastatic potential of cells emanating from the same tumor has been linked to tumor heterogeneity. In addition to this, our results identify two important cell extrinsic factors—extent of confinement and confinement geometry—that influence cancer invasiveness. Our simulations of cell migration through two different channel geometries (tapered and flat) illustrate the importance of confinement geometry in dictating cancer invasiveness. While tapered geometries mediate cell entry into narrow pores by providing cues that enable cells to evolve their shape over time, cells entering channels with flat geometries fail due to absence of appropriate guidance. Given the innate heterogeneity in ECM organization, invasion efficiencies of two cells of identical size and identical cell and nuclear stiffness may vary due to differences in the confinement architecture faced by them. Our study, for the first time, suggests that confinement history influences invasion efficiency by altering entry efficiency. Extent of confinement witnessed by a cell in recent past modulates the extent of cell squeezing; this in-turn influences entry efficiency during entry into subsequent confined regions. Studying the existence of this phenomena represents one of the avenues for further experimental work in this direction.

The effect of ECM confinement on cytoskeletal and nucleoskeletal organization have been demonstrated by various groups (Pathak

variables in a context-dependent manner to optimize invasion (Wolf et al., 2013). Biophysical measurements of cell/nuclear stiffness have demonstrated a strong positive correlation between cell/nuclear deformability (i.e., softness) and malignancy (Willis et al., 2008; Swaminathan et al., 2011; Xu et al., 2012; Harada et al., 2014). Nuclear deformability represents another rate-limiting factor of three-dimensional cell migration, with nuclear softening associated with increased migration (Wolf et al., 2013; Davidson et al., 2014; Krause and Wolf, 2015). Given the strong nucleocytoskeletal coupling in cells, it is experimentally challenging to independently tune cell and nuclear stiffness to understand their individual influence on invasion efficiency. The multicompartment computational modeling framework developed in this study can be a very useful tool to complement experimental studies for identifying the individual contributions of cell/nuclear deformability on cell invasiveness. In our simulations, cell and nuclear properties were tuned by varying perimeter constraint and area constraint. These constructs have been used by different modeling formalisms, including cellular potts models and vertex models with perimeter constraint indicative of line tension and area constraint indicative of bulk stiffness (Fletcher et al., 2013). Our results suggest that, compared with nuclear deformability, cell deformability has a stronger effect on migration efficiency. Though a direct map-

and Kumar, 2012; Davidson *et al.*, 2015). It is possible that these alterations in cell/nuclear properties directly impact the efficiency of cell migration, thereby linking confinement history and invasion efficiency. While no specific mechanism of dynamic tuning of cell/nucleus deformability was considered in this model to maintain generality and to avoid large number of parameters, confinement-dependent rupturing of the nuclear envelope, and its subsequent repair, could be one of the mechanisms for spatiotemporal modulation of nuclear stiffness (Denais *et al.*, 2016; Raab *et al.*, 2016). Similarly, though advancements in technologies facilitating probing of nuclear mechanics have provided significant details about mechanisms of force transmission to nucleus (Kirby and Lammerding, 2018), extending our current model by incorporating these finer details is expected to provide additional insight into how spatiotemporal alterations in nuclear deformability can increase invasion efficiency.

Recently, by studying migration of cells and cytoplasts (i.e., cells from where the nuclei have been removed), Burridge and coworkers demonstrated that the nucleus is a critical component of an integrated molecular clutch that links the nucleus to focal adhesions through the actomyosin cytoskeleton (Graham *et al.*, 2018). Thus, while enucleation (i.e., removal of nucleus) induces loss of contractility (Graham *et al.*, 2018), reduction of ECM stiffness, inhibition of cell contractlity, or disruption of the LINC complex are all expected to induce nuclear softening. Consistent with this idea, ECM stiffness has been shown to regulate nuclear properties by regulating lamin A/C phosphorylation (Buxboim *et al.*, 2014). Since myosin IIB-based contractility is critical for enabling nuclear translocation during three-dimensional invasion (Thomas *et al.*, 2015), it remains to be seen if confined migration can be sustained by a combination of nuclear softening and loss of contractility achieved by transient delinking of the actomyosin cytoskeleton from the nucleus.

In conclusion, this work provides several novel insights into the role of cell and nuclear deformability on cell invasiveness. In addition, our model implicates confinement shape and history as cell extrinsic regulators of invasion efficiency. The model can also be extended to incorporate other aspects of nuclear mechanics. For example, representation of the nucleus as a multicompartment entity can enable us to incorporate mechanical properties of distinct nuclear regions (e.g., nuclear envelope, nucleoplasm) to probe their individual roles in migration. Additionally, incorporation of cytoskeletal dynamics dictated by topographical (e.g., confinement) and chemical cues (e.g., chemokines, calcium) can be pursued as future directions of this work. Construction of a model connecting confinement size/geometry with cell/nuclear deformability that accounts for the integrated molecular clutch is expected to further improve our understanding of confined migration.

MATERIAL AND METHODS
Simulation algorithm
The complete simulation lattice was decomposed into four types of pixels: cytoplasm pixel, nucleus pixel, fluid (free space), and ECM pixel (represent nondeformable confinement). Spatiotemporal evolution of the simulation lattice was governed by random movement of individual pixels subjected to transition probabilities based on the Monte Carlo method (Swat *et al.*, 2012, Kumar *et al.*, 2016). Algorithmically, during each move, two neighboring pixels were chosen randomly, with one designated as the *source* pixel and the other one as the *target* pixel (Supplemental Figure S2A). An attempt to update the lattice was made only when both the *source* and the *target* pixels represented either a cell pixel (i.e., either a nucleus pixel or a cytoplasm pixel) or a fluid pixel, that is, matrix pixels did not participate in the random Monte Carlo updates. As result of this

update, the *source* pixel attempted to occupy the *target* pixel based on Monte Carlo acceptance probability (Supplemental Figure S2B). To do this, the total system energy associated with the configuration before the proposed move (E_i) and the configuration after the proposed move (E_f) were calculated as per the following equation:

$$E_{Total} = \sum_{\forall i,j, i \neq j} J_{\tau(\sigma(i)), \tau(\sigma(j))} + \sum_{\forall c_1, c_2 \in \text{ compartments}} k_{c_1, c_2}(d_{c_1, c_2} - r_{c_1, c_2})^2$$
$$+ \sum_{\forall X \in \text{ compartment}} \lambda_{a,X}(A_X(t) - A_X^0)^2$$
$$+ \sum_{\forall X \in \text{ compartment}} \lambda_{p,X}(P_X(t) - P_X^0)^2$$
$$- \mu_\sigma \times [v(\text{target}) - v(\text{source})] \quad\quad (1)$$

In this expression, $\sigma(i)$ represents the compartment ID of pixel i and $\tau(C)$ represents the type of compartment C. Five different energy terms contribute to the total energy of the system (E_{total}). The first term accounts for the adhesive/repulsive dynamics between different type of compartments (e.g., between a cytoplasmic and nuclear compartment) or two compartments of the same type (e.g., between two cytoplasmic compartments). $J_{t1,t2}$ represents the boundary energy per unit length between compartment of type t_1 and t_2 (e.g., $J_{c,c}$ represents the interface energy per unit length between two adjacent cytoplasmic compartments), with higher value of $J_{X,X}$ indicative of lower adhesion and vice versa (Kumar *et al.*, 2016). While such interface energies have been used to model wide range of phenomena including cell–cell adhesion and cell–ECM adhesion (Kumar *et al.*, 2016), in the current model, we have used this energy term to make sure that the nucleus remains inside the cytoplasm and does not come to the cell surface. This was achieved by assigning very high +ve interface energy for nucleus–matrix and nucleus–medium interfaces (Table 1). Additionally, -ve energies were assigned for cytoplasm–cytoplasm, cytoplasm–nucleus, and nucleus–nucleus interfaces to ensure that the cell cytoplasm and cell nucleus remain connected. The second term in Eq. 1 was included to avoid cell fragmentation by constraining the intercompartment distance between two neighboring compartments. In this term, $k_{c1,c2}$ represents the strength of connectivity, $d_{c1,c2}$ represents the desired distance between center of masses of compartments c_1 and c_2, and $r_{c1,c2}$ represents the Euclidean distance between the center of masses of two compartments. In the third and fourth energy terms, area constraints $\lambda_{a,X}$ and perimeter constraints $\lambda_{p,X}$ were used to avoid excessive deviations in (cytoplasmic and nuclear) compartment areas/perimeters from their preferred area (A_X^0) and their preferred perimeter (P_X^0), respectively. Both area and perimeter constraints control the rigidity of the cytoplasmic/nuclear compartments (Swat *et al.*, 2012), and these parameters were varied to study the effect of cell/nucleus deformability on migration through confined environments. A separate set of simulations was performed to study the influence of area constraint on variation of cell and nuclear area (Supplemental Figure S7, discussed below). Finally, the last term in Eq. 1 was included to model chemotaxis of cells in the direction of the chemoattractant gradient (Davidson *et al.*, 2015). μ_σ encodes effective chemical potential, which influences the strength of chemotaxis relative to other parameters in the model. $v(\text{target})$ and $v(\text{source})$ represent the concentrations of chemoattractant at the *target* and *source* pixels, respectively (Figure 1). While directed migration has been been implemented using multiple approaches including polarization-based rules (Scianna and Preziosi, 2013; Kumar *et al.*, 2016), in this work, we have used a chemotaxis-based

Parameter	Value	Remark
Pixel size	1 μm × 1 μm	Value optimized to balance the trade-off between spatial resolution and simulation complexity.
Total simulation time	40 h	Large enough so cell can transit through a 300-μm-long channel.
k	20 E/L^2	Assumed in the article. Value optimized to make sure that all cell compartments remain connected.
J_{XX}	$(J_{CC}, J_{CN}, J_{NN}, J_{NMat}, J_{NMed})$ = (−50,−50,−60,100,100) E/L	Assumed in the article. Values optimized to ensure that all compartments remain as single entity and nucleus compartment remains inside the cytoplasm compartment.
Perimeter constraint of cytoplasmic compartment ($\lambda_{p,C}$)	2 – 10 E/L^2	Value varied to model extent of cell deformability. See text.
Perimeter constraint of nuclear compartment ($\lambda_{p,N}$)	2 – 20 E/L^2	Value varied to model extent of nuclear deformability. See text.
Area constraint of cytoplasmic compartment ($\lambda_{a,C}$)	2–10 E/L^4	Value varied to model extent of cell deformability. See text.
Area constraint of nuclear compartment ($\lambda_{a,N}$)	2–20 E/L^4	Value varied to model extent of cell deformability. See text.
Equilibrium compartment area (A_X^0)	25 μm^2	Value determined based on experimental data which show that cell area is in the range 200–270 μm^2 (Supplemental Figure S1, A and B).
Equilibrium compartment perimeter (P_X^0)	17.72 μm	Value calculated by assuming that each compartment is circular in shape.
Strength of chemotaxis force (μ_σ)	5000	Assumed in this article.
$\hat{p}$	i+0.j	Unit vector in +ve x-direction to make sure that a cell moves through the channel.
T_m	10 E	Value assumed in the model to balance the trade-off between simulation time and noise level. See text.

E and L represent the energy and length dimensions, respectively. L is 1 μm in our study.

TABLE 1: Values of parameters used in simulations.

approach that closely mimics the experimental setup developed by Piel and coworkers (Davidson *et al.*, 2015).

Once the total energy of the system before the move (E_i) and after the move (E_f) were determined, the probability (ρ) of accepting the move was calculated as per the expression p =1 if (E_f–$E_i \leq 0$). Else, $p = e^{-(E_f - E_i)/(k_B T_m)}$ if E_f–$E_i > 0$ (Supplemental Figure S2B). Boltzmann acceptance function-based stochastic evolution of the system using this probabilistic approach tries to drive the system towards a state with lower energy (Metropolis *et al.*, 1953). In CPM, T_m represents the strength of noise in the dynamics or magnitude of effective membrane fluctuations. While increase in T_m increases the chances of accepting an unfavorable move and increases stochasticity in the simulations, lower values of T_m make the system highly deterministic (Swat *et al.*, 2012). Last, each Monte Carlo step (MCS) corresponded to repeating this exercise N times (N being the total number of lattice pixels that can be evolved) irrespective of whether the moves were accepted or not.

Parameter values and model assumptions

All parameter values used in the model were either taken from the literature or were chosen based on our own experiments. The values of the model parameters are listed in Table 1 and the rationales behind these values are as follows:

1. Based on experiments with MDA-MB-231 human breast cancer cells, the total cell area was estimated to be ≈225 μm^2 (Supplemental Figure S1, A and B). Since a single cell is composed of nine compartments, each compartment size was chosen to be 25 μm^2. From this size, we calculated the perimeter of each compartment to be ≈17.72 μm (=$2 * \pi * \sqrt{25/\pi}$) by assuming that each compartment is circular in shape. Further, since the length scales of all entities are in multiples of μm and smallest length scale involved in our system is 3 μm (size of narrowest channel), we chose 1 pixel to be equivalent to 1 μm × 1 μm.

2. Based on our experimental observations where we observed a higher nuclear stiffness (2–6 kPa) than cell stiffness (0.5–2.5 kPa) for MDA-MB-231 cells (Supplemental Figure S1, C–E), we assumed $\lambda_{p,C} \leq \lambda_{p,N}$ in our simulations with max($\lambda_{p,C}$) = 0.5 × max ($\lambda_{p,N}$).

3. Values of adhesion energies ($J_{X,X}$) and elastic constant (k) were chosen to ensure that the nucleus remained inside the cell body and the cell compartments remained attached to each other.

4. A separate set of simulations with various area constraints (λ_a) and perimeter constraint (λ_a) was also performed to assess the importance of these parameter in our simulations (Supplemental Figure S7). In these simulations, cells were placed in unconfined environment and cell/nuclear area was quantified at every MCS.

5. The magnitude of effective membrane fluctuations (T_m) and chemotaxis strength (μ_σ) were assumed in our model. Since both T_m and μ_σ parameters (i.e., their relatives value with respect to other parameters) influence cell motility (Kabla, 2012; Swat *et al.*, 2012), we collectively tuned these parameters to balance the trade-off between simulation time and noise in the system. While very low values of T_m and μ_σ freezes the cell movement thereby requiring significantly large number of MCS to simulate cell

movement through the channel, very high values of T_m is expected to increase the noise in the system (Swat *et al.*, 2012).

6. To determine the value of one simulation step (1 MCS), we quantified the speed of the MDA-MB-231 cells migrating on two-dimensional gels and compared that speed with the speed of simulated cells when migrating through the least confined environment, that is, $\phi = 17$ μm. This comparison was performed at moderate values of cell and nuclear stiffness, that is, $\lambda_{p,C} = \lambda_{p,N} = 5\ E/L^2$. In simulation, cells with $\lambda_{p,C} = \lambda_{p,N} = 5\ E/L^2$ transited through a 300-μm-long channel in 15,000 MCS, thereby giving a speed of 0.02 μm/MCS. On comparing this speed with experimentally observed speed of MDA-MB-231, that is, ~10 μm/h (Supplemental Figure S8), we obtain 1 MCS = $\approx$7 s.

7. Last, perimeter and area constraints of cytoplasm and nucleus compartments were varied in our study to explore the effect of cell and nuclear deformability on cell invasiveness.

Simulation implementation, visualization and data analysis

The complete simulation framework was implemented using the open-source package CompuCell3D (CC3D) (Swat *et al.*, 2012). Additional code scripts were written in Python to implement custom routines. Detailed description of the simulation implementation is provided in the Supplemental text. For visualization, *.vtk files were generated from the CC3D simulations and visualized in Paraview software (Ahrens *et al.*, 2005). For quantifying migration trajectories, cell centroid was tracked and logged to CSV files. These files were then processed in Matlab using custom-written Matlab scripts to extract different invasiveness metrics.

Code availability

CC3D code used to implement the complete model will be available to interested researchers upon request. Such requests can be sent to the corresponding author.

REFERENCES

Ahrens J, Geveci B, Law C (2005). Paraview: An end-user tool for large-data visualization. In: The Visualization Handbook, ed. CD Hansen and CR Johnson, Elsevier Butterworth-Heinemann, 717–731.

Albert PJ, Schwarz US (2016). Dynamics of cell ensembles on adhesive micropatterns: bridging the gap between single cell spreading and collective cell migration. PLoS Comput Biol 12, e1004863.

Alexander S, Weigelin B, Winkler F, Friedl P (2013). Preclinical intravital microscopy of the tumour-stroma interface: invasion, metastasis, and therapy response. Curr Opin Cell Biol 25, 659–671.

Balzer EM, Tong Z, Paul CD, Hung WC, Stroka KM, Boggs AE, Martin SS, Konstantopoulos K (2012). Physical confinement alters tumor cell adhesion and migration phenotypes. FASEB J 26, 4045–4056.

Bauer AL, Jackson TL, Jiang Y (2009). Topography of extracellular matrix mediates vascular morphogenesis and migration speeds in angiogenesis. PLoS Comput Biol 5, e1000445.

Boghaert E, Radisky DC, Nelson CM (2014). Lattice-based model of ductal carcinoma in situ suggests rules for breast cancer progression to an invasive state. PLoS Comput Biol 10, e1003997.

Buxboim A, Swift J, Irianto J, Spinler KR, Dingal PD, Athirasala A, Kao YR, Cho S, Harada T, Shin JW, Discher DE (2014). Matrix elasticity regulates lamin-A, C phosphorylation and turnover with feedback to actomyosin. Curr Biol 24, 1909–1917.

Caballero D, Comelles J, Piel M, Voituriez R, Riveline D (2015). Ratchetaxis: long-range directed cell migration by local cues. Trends Cell Biol 25, 815–827.

Cano ML, Lauffenburger DA, Zigmond SH (1991). Kinetic analysis of F-actin depolymerization in polymorphonuclear leukocyte lysates indicates that chemoattractant stimulation increases actin filament number without altering the filament length distribution. J Cell Biol 115, 677–687.

Dahl KN, Ribeiro AJ, Lammerding J (2008). Nuclear shape, mechanics, and mechanotransduction. Circ Res 102, 1307–1318.

Davidson PM, Denais C, Bakshi MC, Lammerding J (2014). Nuclear deformability constitutes a rate-limiting step during cell migration in 3-d environments. Cell Mol Bioeng 7, 293–306.

Davidson PM, Sliz J, Isermann P, Denais C, Lammerding J (2015). Design of a microfluidic device to quantify dynamic intra-nuclear deformation during cell migration through confining environments. Integr Biol (Camb) 7, 1534–1546.

Denais CM, Gilbert RM, Isermann P, McGregor AL, te Lindert M, Weigelin B, Davidson PM, Friedl P, Wolf K, Lammerding J (2016). Nuclear envelope rupture and repair during cancer cell migration. Science 352, 353–358.

Desai SP, Bhatia SN, Toner M, Irimia D (2013). Mitochondrial localization and the persistent migration of epithelial cancer cells. Biophys J 104, 2077–2088.

Doxzen K, Vedula SRK, Leong MC, Hirata H, Gov NS, Kabla AJ, Ladoux B, Lim CT (2013). Guidance of collective cell migration by substrate geometry. Integr Biol (Camb) 5, 1026–1035.

Fletcher AG, Osborne JM, Maini PK, Gavaghan DJ (2013). Implementing vertex dynamics models of cell populations in biology within a consistent computational framework. Prog Biophys Mol Biol 113, 299–326.

Franz CM, Jones GE, Ridley AJ (2002). Cell migration in development and disease. Dev Cell 2, 153–158.

Friedl P, Wolf K (2009). Proteolytic interstitial cell migration: a five-step process. Cancer Meta Rev 28, 129–135.

Friedl P, Wolf K (2010). Plasticity of cell migration: a multiscale tuning model. J Cell Biol 188, 11–19.

Goldman RD, Shumaker DK, Erdos MR, Eriksson M, Goldman AE, Gordon LB, Gruenbaum Y, Khuon S, Mendez M, Varga R, *et al.* (2004). Accumulation of mutant lamin a causes progressive changes in nuclear architecture in hutchinson–gilford progeria syndrome. Proc Natl Acad Sci USA 101, 8963–8968.

Graham DM, Andersen T, Sharek L, Uzer G, Rothenberg K, Hoffman BD, Rubin J, Balland M, Bear JE, Burridge K (2018). Enucleated cells reveal differential roles of the nucleus in cell migration, polarity, and mechanotransduction. J Cell Biol 217, 895–914.

Harada T, Swift J, Irianto J, Shin JW, Spinler KR, Athirasala A, Diegmiller R, Dingal PDP, Ivanovska IL, Discher DE (2014). Nuclear lamin stiffness is a barrier to 3D migration, but softness can limit survival. J Cell Biol 204, 669–682.

Hung WC, Yang JR, Yankaskas CL, Wong BS, Wu PH, Pardo-Pastor C, Serra SA, Chiang MJ, Gu Z, Wirtz D, *et al.* (2016). Confinement sensing and signal optimization via piezo1/pka and myosin ii pathways. Cell Rep 15, 1430–1441.

Irimia D, Toner M (2009). Spontaneous migration of cancer cells under conditions of mechanical confinement. Integr Biol (Camb) 1, 506–512.

Kabla AJ (2012). Collective cell migration: leadership, invasion and segregation. J R Soc Interface 9, 3268–3278.

Käfer J, Hayashi T, Marée AF, Carthew RW, Graner F (2007). Cell adhesion and cortex contractility determine cell patterning in the drosophilaretina. Proc Natl Acad Sci USA 104, 18549–18554.

Kirby TJ, Lammerding J (2018). Emerging views of the nucleus as a cellular mechanosensor. Nat Cell Biol 20, 373–381.

Krause M, te Riet J, Wolf K (2013). Probing the compressibility of tumor cell nuclei by combined atomic force–confocal microscopy. Phys Biol 10, 065002.

Krause M, Wolf K (2015). Cancer cell migration in 3D tissue: negotiating space by proteolysis and nuclear deformability. Cell Adh Migr 9, 357–366.

Kumar S, Kapoor A, Desai S, Inamdar MM, Sen S (2016). Proteolytic and non-proteolytic regulation of collective cell invasion: tuning by ecm density and organization. Sci Rep 6, 19905.

Lammerding J, Fong LG, Ji JY, Reue K, Stewart CL, Young SG, Lee RT (2006). Lamins A and C but not lamin B1 regulate nuclear mechanics. J Biol Chem 281, 25768–25780.

Lammerding J, Schulze PC, Takahashi T, Kozlov S, Sullivan T, Kamm RD, Stewart CL, Lee RT (2004). Lamin A/C deficiency causes defective nuclear mechanics and mechanotransduction. J Clin Inv 113, 370–378.

Lämmermann T, Sixt M (2009). Mechanical modes of 'amoeboid' cell migration. Curr Opin Cell Biol 21, 636–644.

Lautscham LA, Kämmerer C, Lange JR, Kolb T, Mark C, Schilling A, Strissel PL, Strick R, Gluth C, Rowat AC, et al. (2015). Migration in confined 3D environments is determined by a combination of adhesiveness, nuclear volume, contractility, and cell stiffness. Biophys J 109, 900–913.

Le Berre M, Liu YJ, Hu J, Maiuri P, Bénichou O, Voituriez R, Chen Y, Piel M (2013). Geometric friction directs cell migration. Phys Rev Lett 111, 198101.

Licup AJ, Münster S, Sharma A, Sheinman M, Jawerth LM, Fabry B, Weitz DA, MacKintosh FC. (2015). Stress controls the mechanics of collagen networks. Proc Natl Acad Sci USA 112, 9573–9578.

Luxton GG, Gundersen GG (2011). Orientation and function of the nuclear–centrosomal axis during cell migration. Curr Opin Cell Biol 23, 579–588.

McGregor AL, Hsia CR, Lammerding J (2016). Squish and squeeze—the nucleus as a physical barrier during migration in confined environments. Curr Opin Cell Biol 40, 32–40.

Metropolis N, Rosenbluth AW, Rosenbluth MN, Teller AH, Teller E. (1953). Equation of state calculations by fast computing machines. J Chem Phys 21, 1087–1092.

Miller PM, Folkmann AW, Maia AR, Efimova N, Efimov A, Kaverina I (2009). Golgi-derived CLASP-dependent microtubules control Golgi organization and polarized trafficking in motile cells. Nat Cell Biol 11, 1069.

Muller N, Piel M, Calvez V, Voituriez R, Gonçalves-Sá J, Guo CL, Jiang X, Murray A, Meunier N (2016). A predictive model for yeast cell polarization in pheromone gradients. PLoS Comput Biol 12, e1004795.

Murrell MP, Gardel ML (2012). F-actin buckling coordinates contractility and severing in a biomimetic actomyosin cortex. Proc Natl Acad Sci USA 109, 20820–20825.

Nemere I, Kupfer A, Singer SJ (1985). Reorientation of the Golgi apparatus and the microtubule organizing center inside macrophages subjected to a chemotactic gradient. Cytoskeleton 5, 17–29.

Pajerowski JD, Dahl KN, Zhong FL, Sammak PJ, Discher DE (2007). Physical plasticity of the nucleus in stem cell differentiation. Proc Natl Acad Sci USA 104, 15619–15624.

Pankov R, Endo Y, Even-Ram S, Araki M, Clark K, Cukierman E, Matsumoto K, Yamada KM (2005). A Rac switch regulates random versus directionally persistent cell migration. J Cell Biol 170, 793–802.

Pathak A, Kumar S (2012). Independent regulation of tumor cell migration by matrix stiffness and confinement. Proc Natl Acad Sci USA 109, 10334–10339.

Paul CD, Shea DJ, Mahoney MR, Chai A, Laney V, Hung WC, Konstantopoulos K (2016). Interplay of the physical microenvironment, contact guidance, and intracellular signaling in cell decision making. FASEB J 30, 2161–2170.

Plodinec M, Loparic M, Monnier CA, Obermann EC, Zanetti-Dallenbach R, Oertle P, Hyotyla JT, Aebi U, Bentires-Alj M, Lim RY, et al. (2012). The nanomechanical signature of breast cancer. Nat Nanotechnol 7, 757–765.

Pouthas F, Girard P, Lecaudey V, Ly TB, Gilmour D, Boulin C, Pepperkok R, Reynaud EG (2008). In migrating cells, the Golgi complex and the position of the centrosome depend on geometrical constraints of the substratum. J Cell Sci 121, 2406–2414.

Raab M, Gentili M, de Belly H, Thiam HR, Vargas P, Jimenez AJ, Lautenschlaeger F, Voituriez R, Lennon-Duménil AM, Manel N, Piel M (2016). ESCRT III repairs nuclear envelope ruptures during cell migration to limit DNA damage and cell death. Science 352, 359–362.

Roussos ET, Condeelis JS, Patsialou A (2011). Chemotaxis in cancer. Nat Rev Cancer 11, 573–587.

Rowat AC, Jaalouk DE, Zwerger M, Ung WL, Eydelnant IA, Olins DE, Olins AL, Herrmann H, Weitz DA, Lammerding J (2013). Nuclear envelope composition determines the ability of neutrophil-type cells to passage through micron-scale constrictions. J Biol Chem 288, 8610–8618.

Scherber C, Aranyosi AJ, Kulemann B, Thayer SP, Toner M, Iliopoulos O, Irimia D (2012). Epithelial cell guidance by self-generated EGF gradients. Integr Biol 4, 259–269.

Scianna M, Preziosi L (2013). Modeling the influence of nucleus elasticity on cell invasion in fiber networks and microchannels. J Theor Biol 317, 394–406.

Sottoriva A, Vermeulen L, Tavaré S (2011). Modeling evolutionary dynamics of epigenetic mutations in hierarchically organized tumors. PLoS Comput Biol 7, e1001132.

Stroka KM, Jiang H, Chen SH, Tong Z, Wirtz D, Sun SX, Konstantopoulos K (2014). Water permeation drives tumor cell migration in confined microenvironments. Cell 157, 611–623.

Swaminathan V, Mythreye K, O'Brien ET, Berchuck A, Blobe GC, Superfine R (2011). Mechanical stiffness grades metastatic potential in patient tumor cells and in cancer cell lines. Cancer Res 71, 5075–5080.

Swat MH, Thomas GL, Belmonte JM, Shirinifard A, Hmeljak D, Glazier JA (2012). Multi-scale modeling of tissues using CompuCell3D. Methods Cell Biol 110, 325–366.

Szabó A, Merks RM (2013). Cellular potts modeling of tumor growth, tumor invasion, and tumor evolution. Front Oncol 3, 87.

Szabó A, Varga K, Garay T, Hegedüs B, Czirók A (2012). Invasion from a cell aggregate—the roles of active cell motion and mechanical equilibrium. Phys Biol 9, 016010.

Thomas DG, Yenepalli A, Denais CM, Rape A, Beach JR, Wang YL, Schiemann WP, Baskaran H, Lammerding J, Egelhoff TT (2015). Non-muscle myosin IIB is critical for nuclear translocation during 3D invasion. J Cell Biol 210, 583–594.

Vedula SRK, Leong MC, Lai TL, Hersen P, Kabla AJ, Lim CT, Ladoux B (2012). Emerging modes of collective cell migration induced by geometrical constraints. Proc Natl Acad Sci USA 109, 12974–12979.

Verstraeten VL, Ji JY, Cummings KS, Lee RT, Lammerding J (2008). Increased mechanosensitivity and nuclear stiffness in hutchinson–gilford progeria cells: effects of farnesyltransferase inhibitors. Aging Cell 7, 383–393.

Vogel SK, Petrasek Z, Heinemann F, Schwille P (2013). Myosin motors fragment and compact membrane-bound actin filaments. Elife 2, e00116.

Weigelin B, Bakker GJ, Friedl P (2012). Intravital third harmonic generation microscopy of collective melanoma cell invasion: principles of interface guidance and microvesicle dynamics. IntraVital 1, 32–43.

Willis ND, Cox TR, Rahman-Casans SF, Smits K, Przyborski SA, van den Brandt P, van Engeland M, Weijenberg M, Wilson RG, De Brune A, et al. (2008). Lamin a/c is a risk biomarker in colorectal cancer. PLoS One 3, e2988.

Wolf K, Mazo I, Leung H, Engelke K, Von Andrian UH, Deryugina EI, Strongin AY, Bröcker EB, Friedl P (2003). Compensation mechanism in tumor cell migration mesenchymal—amoeboid transition after blocking of pericellular proteolysis. J Cell Biol 160, 267–277.

Wolf K, Te Lindert M, Krause M, Alexander S, Te Riet J, Willis AL, Hoffman RM, Figdor CG, Weiss SJ, Friedl P (2013). Physical limits of cell migration: control by ecm space and nuclear deformation and tuning by proteolysis and traction force. J Cell Biol 201, 1069–1084.

Wolf K, Wu YI, Liu Y, Geiger J, Tam E, Overall C, Stack MS, Friedl P (2007). Multi-step pericellular proteolysis controls the transition from individual to collective cancer cell invasion. Nat Cell Biol 9, 893–904.

Xu W, Mezencev R, Kim B, Wang L, McDonald J, Sulchek T (2012). Cell stiffness is a biomarker of the metastatic potential of ovarian cancer cells. PLoS One 7, e46609.

Yvon AM, Walker JW, Danowski B, Fagerstrom C, Khodjakov A, Wadsworth P (2002). Centrosome reorientation in wound-edge cells is cell type specific. Mol Biol Cell 13, 1871–1880.